University of New Mexico
UNM Digital Repository

Mechanical Engineering ETDs | Engineering ETDs

Summer 7-30-2024

Tuning of Real-time Optimization of Heliostat Concentrated Solar Power

Zachary L. Bernius
University of New Mexico

Follow this and additional works at: https://digitalrepository.unm.edu/me_etds

 Part of the Acoustics, Dynamics, and Controls Commons

Recommended Citation

Bernius, Zachary L.. "Tuning of Real-time Optimization of Heliostat Concentrated Solar Power." (2024). https://digitalrepository.unm.edu/me_etds/268

This Thesis is brought to you for free and open access by the Engineering ETDs at UNM Digital Repository. It has been accepted for inclusion in Mechanical Engineering ETDs by an authorized administrator of UNM Digital Repository. For more information, please contact disc@unm.edu.

Zachary Bernius

Candidate

Mechanical Engineering

Department

This thesis is approved, and it is acceptable in quality and form for publication:

Approved by the Thesis Committee:

Dr. Claus Danielson, Chair

Dr. Meeko Oishi

Dr. Kenneth Armijo

TUNING OF REAL-TIME OPTIMIZATION OF HELIOSTAT CONCENTRATED SOLAR POWER

BY

ZACHARY LEE BERNIUS
B.S. Mechanical Engineering, University of New Mexico,
2023

THESIS

Submitted in Partial Fulfillment
of the Requirements for the Degree of

Master of Science

Mechanical Engineering

The University of New Mexico
Albuquerque, New Mexico

JULY 2024

DEDICATION

I dedicate this work to Micah Mueller, for all of her love and support throughout this accomplishment.

ACKNOWLEDGMENTS

There are many people that need to be acknowledged. First, I would like to thank my friends and family who supported me and encouraged me to take on this challenge. Second, I would like to thank my advisor, Dr. Claus Danielson, for his guidance. I would not have been able to complete this research without him. Third, I would like to thank Dr. Kenneth Armijo, Luis Maldonado, and Dr. Aaron Overacker at the NSTTF and Dr. Meeko Oishi for their guidance and for bridging the gaps in my understanding. Lastly, I would like to thank my fellow students in Dr. Danielson's lab, especially Haden Harper, who helped me refine my knowledge on this topic.

Tuning of Real-Time Optimization of Heliostat Concentrated Solar Power

by

Zachary Lee Bernius

B.S. Mechanical Engineering, University of New Mexico, 2023

M.S. Mechanical Engineering, University of New Mexico, 2024

ABSTRACT

This paper investigates a real-time optimization algorithm for autonomously calibrating the heliostats in a concentrated solar power plant with the goal of maximizing power generation. The current state-of-the-art uses human operators to provide feedback for the heliostats. We use real-time/online measurements to produce an autonomous closed-loop system that does not require human intervention. The paper investigates tuning the gain of the real-time optimization algorithm to quickly and robustly converge to the optimal alignment and stabilize the system. The exponential stability of the system is certified using a quadratic Lyapunov function and static output feedback methods to couple the Lyapunov functions of the plant and the controller. To validate stability, performance, and robustness, the algorithm is simulated using different power distributions and gains, as well as tested using an actual heliostat, that show the need for the real-time optimization algorithm.

TABLE OF CONTENTS

1 Introduction

Concentrated Solar Power (CSP) is among the most reliable forms of renewable energy and can rival non-renewable sources [10] by using reflected sunlight to generate power [16]. Another well-known method for energy production using the Sun is photovoltaics, or solar panels. While both CSP and solar panels use sunlight for producing power, these methods differ in how the sunlight is used. Solar panels absorb sunlight directly to transform the energy into electricity [2]. A CSP plant concentrates solar energy to heat a working fluid which is used in a traditional thermodynamic cycle to produce electricity. This has three main advantages. First, while the power capacity varies as a function of time of year and time of day, CSP is available regardless of the time of year. Second, CSP uses concentrated sunlight to heat a working fluid, enabling thermal storage which can be used to continuously generate power, even at night. Third, reflecting sunlight to heat a working fluid provides a more efficient mechanism for transforming solar energy. There are several different mechanisms for concentrating solar power in CSP, including fresnel lenses [15], through parabolic dishes [12], and power towers that use heliostats, which are considered in this paper. A heliostat is a collection of mirrors (referred to as facets), that reflects sunlight onto a power tower, also known as the receiver, to heat the working fluid. A challenge of CSP using heliostats is the high initial costs of building the plant. Another challenge with heliostats is that they require control systems for alignment and pointing.

The Carnot efficiency of power generation increases with the heat-flux on the receiver. Thus, to maximize power generation, the heliostats need to continually realign with the Sun's movement to reflect sunlight optimally onto the power tower. Ideally, this realignment can be performed autonomously using Real-time Optimization (RTO) [6] to find and maintain the optimal pointing alignment.

Currently, the desired alignment is facilitated by open-loop controls from a human-operator in the form of an azimuth and an elevation angle tracked by the heliostats. The open-loop azimuth and elevation angle set-points are computed using the current position of the Sun, the position of the mirror, and the position of the receiver. An inner-loop controller tracks the desired azimuth and elevation angle to move the heliostats to their actual azimuth and elevation angle. This differs from the outer-loop feedback controller mentioned in later sections, which selects the desired azimuth and elevation angle in real-time to maximize power.

There are several issues with the current open-loop approach that unnecessarily reduce power generation. First, model uncertainty introduces error, resulting in misalignment of the sunspot on the receiver. This is introduced by misalignment of coordinate frames between the heliostat and the receiver. Essentially, the blueprint location and orientation of the heliostat differs from its actual location and orientation, leading to misalignment in the absence of corrective feedback. In addition, miscalibration of the encoders used by the inner-loop heliostat controllers can result in the heliostat reflecting sunlight in an unintended direction. Second, the heliostats do not track the Sun perfectly to adjust to the Sun's movement. Slight tracking error causes the sunspot to gradually drift away from the desired position. This requires the operator to continuously monitor and adjust commands to the heliostats. Third, there are disturbances that impact the heliostats, such as wind, which can misalign them. Lastly, another disadvantage of this human-in-the-loop approach is that it requires the constant intervention of a skilled operator. This experienced operator must be paid to estimate the desired alignment and pointing of the heliostats. To address these issues, this paper presents a RTO algorithm for autonomously aligning the heliostats in a CSP plant to maximize power generation despite model uncertainty and disturbances using real-time feedback.

Other methods have been proposed for real-time maximization of power genera-

tion in CSP. A commonly used method is System Observation for Heliostat Orientations while Tracking (SOHOT) [8]. This method uses drones to take images of the heliostats and ray-tracing programs to calculate the heliostats' optimal pointing alignment and then adjusts the alignment to correct the alignment errors. However, this method is time-consuming and expensive. Furthermore, it does not address the need for autonomous feedback, instead provides more data to the human-operator and relies on them to adjust the alignment, increasing their workload and the skill-level necessary to operate the CSP plant. In contrast, the method presented in this paper is less expensive since it uses power measurements from existing sensor infrastructure. Furthermore, our motivation for tuning the RTO controller is to reduce the time required to find the optimal pointing alignment of a heliostat. There is also the advantage of being conceptually simple, using power measurements directly from the receiver. There have also been other closed-loop control approaches done by Kribus et al. in [7] and by Freeman et al. in [4]. The method in [7] compares four images around the receiver to measure sunlight spillage and uses it as feedback to adjust the heliostat. The work in [4] builds upon [7] by using a small mechanical vibration to perturb the light waves that are picked up by photo-sensors around the receiver along with calculating the heliostat's surface normal vector to improve calibration and standalone movement. Our method differs because we use real-time measurements and a gradient ascent algorithm to maximize power. An advantage of our data-driven method is that it is compatible with a variety of data collection methods commonly used by existing CSP plants. Another advantage of our method is that it filters the sensors' measurement to obtain a robust estimate of the optimal pointing alignment of the heliostats whereas other methods assume that the sensor measurements obtained by specialized sensors are truth. Lastly, our method does not require us to calculate the optimal pointing alignment vector.

There are many advantages to closing the loop for real-time heliostat alignment.

First, feedback improves robustness to model uncertainty. Second, feedback improves tracking by minimizing drift from the optimal pointing alignment. Third, feedback allows the heliostat to respond faster to disturbances. Lastly, the closed-loop approach does not require an operator to move the heliostats after the initial desired azimuth and elevation angle.

This paper adopts a standard RTO architecture [11] which is applied to the problem of aligning the CSP heliostats in real-time. The focus of this paper is on tuning the gain of the RTO to provide exponential stability, reduce alignment time, and improve robustness to model uncertainty. Tuning the gain is imperative for several reasons. First, if the wrong gain is used then the closed-loop comprised of the RTO controller and heliostat will become unstable. Second, even when the closed-loop is stable, a mistuned gain could cause the RTO to drive the heliostat into a misaligned equilibrium that reduces power generation. Third, the tuning of the RTO affects the closed-loop settling time of the heliostat. Reducing the settling time will improve tracking of the Sun and rejection of disturbances such as wind. Finally, a properly tuned gain can improve robustness to model uncertainty, in particular the sunspot shape produced by the heliostat facets.

We present a semi-definite programming (SDP) approach for tuning the gain of the RTO. We exploit the fact that the heliostat and power tower CSP plant can be modeled as a Hammerstein system with an exponential non-linearity. Thus, by taking the logarithm of power, the closed-loop system becomes an uncertain linear system. This allows us to adapt semi-definite programming techniques for designing output feedback controllers to tune the RTO for performance and robustness. The SDP problem has linear matrix inequality (LMI) constraints which restrict the optimization to stabilizing gains. These constraints are parameterized for robustness to the unknown shape of the sunspot produced by the heliostat facets. The cost of the SDP problem minimizes the settling-time of the closed-loop system.

The remainder of this paper is organized as follows. In Section 2, we formally define the heliostat alignment problem. In Section 3, we present our approach for tuning the RTO gain to optimize performance and robustness. Finally, in Section 4, we present numerical simulations that demonstrate the effectiveness of our approach.

1.1 Notation and Definitions

The convex hull is defined as

$$\mathcal{C} = \left\{ \sum_{i=1}^{N} \xi_i \Delta_i : \sum_{i=1}^{N} \xi_i = 1, \xi_i \geq 0 \right\} \tag{1}$$

where N is the number of vertices and Δ_i are the vertices of the convex hull.

2 RTO Tuning Problem

In this section, we describe the heliostat alignment problem and the architecture of the RTO we will employ to solve this problem. The block diagram of a heliostat-CSP in closed-loop with a RTO controller is shown in Fig. 1. In the subsequent sections, we will describe the components of the block diagram.

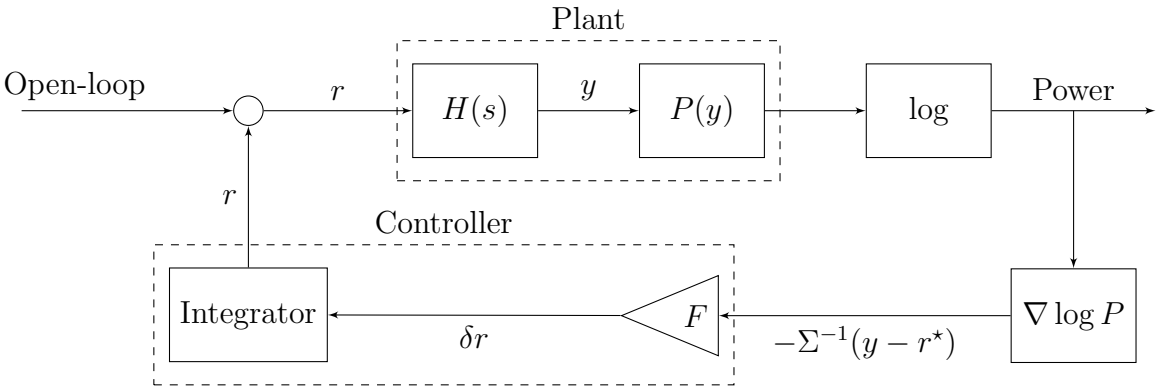

Figure 1: Closed-loop Block Diagram. This figure shows the components of the closed-loop block diagram: the plant, the estimator, and the RTO controller. The figure also shows the connections between each component.

2.1 Heliostat Dynamics

The plant is modeled as a Hammerstein system consisting of the heliostat dynamics and a nonlinear power function. The heliostat is modeled as a known linear system with generic state-space realization

$$x_{k+1} = Ax_k + Br_k \tag{2a}$$

$$y_k = Cx_k \tag{2b}$$

where $x_k \in \mathbb{R}^n$ is the state, and $r_k \in \mathbb{R}^2$ and $y_k \in \mathbb{R}^2$ are the desired and actual heliostat alignments, respectively, at time k. The heliostat dynamics are inherently multi-input/multi-output where the inputs $r = (r_{az}, r_{el}) \in \mathbb{R}^2$ are the desired azimuth r_{az} and elevation angle r_{el} of the heliostat and the outputs $y = (y_{az}, y_{el}) \in \mathbb{R}^2$ are the actual azimuth y_{az} and elevation angle y_{el} measured by the encoders on the heliostat. The heliostats are servo-ed by an inner-loop controller that ensures that measured outputs y converge $y \to r$ to the desired outputs r. This means that the steady-state gain $C(I - A)^{-1}B = I$ is identity. Furthermore, this means that the heliostat dynamics (2) are Schur stable. The objective of this paper is to compute the set-point r which maximizes power generation.

2.2 Power Function

The heliostat reflects a beam of sunlight onto the receiver. The intensity of light across this beam has a Gaussian distribution [14]

$$P(y) = \frac{\bar{P}}{\sqrt{(2\pi)^2|\Sigma|}} \exp\left(-\frac{1}{2}(y - r^*)^T\Sigma^{-1}(y - r^*)\right) \tag{3}$$

where the unknown matrix $\Sigma^{-1} \in \mathbb{R}^{2\times 2}$ determines the shape of the sunspot created by the heliostat, $r^\star \in \mathbb{R}^2$ is the unknown optimal pointing alignment of the heliostat

that maximizes the reflected sunlight on the receiver, $\bar{P}$ is the power provided by the Sun, and $y \in \mathbb{R}^2$ is the azimuth and elevation angle of the heliostat according to (2). The unknown optimal pointing alignment $r^\star$ of the heliostat has a complicated dependence on the relative positions of the Sun, heliostat, and receiver.

The shape matrix $\Sigma^{-1} = \begin{bmatrix} \sigma_{11} & \sigma_{12} \\ \sigma_{12} & \sigma_{22} \end{bmatrix}$ is the main source of uncertainty in the heliostat alignment problem. While we do not know the true value of the shape matrix Σ^{-1}, we have access to sensors that can measure the power $P_k = P(y_k)$ for the current alignment y_k of the heliostat (2). The RTO will use these real-time power measurements to estimate the heliostat's optimal pointing alignment $r^\star$. We model the uncertainty of the power function (3) as a convex hull of the shape matrices Σ^{-1}

$$\mathcal{D} = \left\{ \sum_{i=1}^{N} \xi_i \Sigma_i^{-1} : \sum_{i=1}^{N} \xi_i = 1, \xi_i \geq 0 \right\} \tag{4}$$

The vertices Σ_i^{-1} of the set (4) are empirically gathered from images of the sunspots created by heliostats on the receiver. With thousands of images, each gathered sunspot shape is not necessarily a vertex of the set (4), but are still contained within the set (4).

The set (4) will be used to tune the RTO gain to ensure robustness to the shape of the sunspot.

A major source of noise is the time-varying nominal power $\bar{P}_k$ provided by the Sun. For instance, when the Sun disappears behind a cloud, the nominal power $\bar{P}_k$ will decrease. By taking the logarithm of power (3), we obtain

$$\log P(y) = \log \bar{P}_k - (y - r^\star)^T \Sigma^{-1} (y - r^\star)$$

where $\nu_k = \log \bar{P}_k$ is considered as an additive disturbance, that is independent of the alignment y of the heliostats. Furthermore, when we take the gradient $\nabla_y \log P(y)$

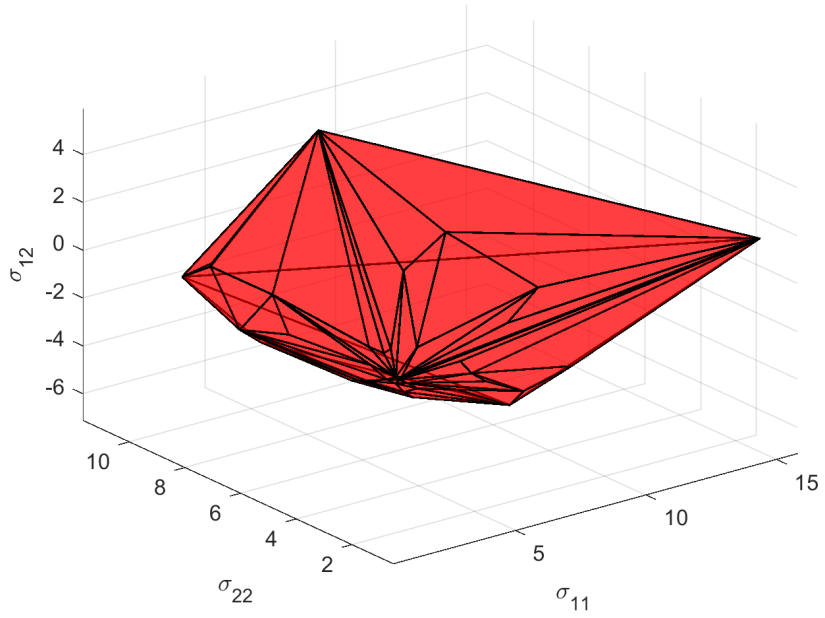

Figure 2: Conceptual Convex Hull. This figure is meant to illustrate what the convex hull using heliostat-receiver data would look like. This figure is generated using 100 different shape matrices Σ^{-1}.

of the log-power with respect to alignment, this term disappears. We assume that the noise $\nu_k = \log \bar{P}_k$ is slowly varying with respect to the gathered data. The change in the Sun's location is also treated as a disturbance. The goal is to reject these disturbances and track an unknown output that maximizes power.

2.3 Gradient Estimator

Since the parameters $\bar{P}$, $r^\star$, and Σ^{-1} of the power function (3) are unknown (and slowly varying), the RTO uses gradient ascent to iteratively find the optimal pointing alignment $r^\star$. This requires a data-driven algorithm for estimating the gradient $\nabla \log P(y)$ of the power function (3). To estimate the gradient, a data-set is constructed from real-time power measurements $\log P_k = \log P(y_k)$ gathered at different locations y_k over time k. These power measurements are taken from the receiver via sensors or images. One of the advantages of using the RTO is that this

data can take the form of temperature, heat-flux, light intensity, or other forms that are representative to power generation. A variety of methods can be used to estimate the gradient $\nabla \log P(y)$ [5] from the data-set $\{y_k, \log P_k\}$. One common method to estimate the gradient is using e.g. batch least squares (BLS) [1]. Since the focus of this paper is on tuning the RTO gain, we assume that the gradient is estimated without error. This is a reasonable assumption since CSP plants tend to be well instrumented due to their expense in commissioning. Due to the ability to use many sensors, such as multiple thermocouples and millions of pixels in BCS images, as well as a relatively large window of time to make measurements due to the slow movement of the Sun and clouds, we are estimating the gradient with millions of power samples.

2.4 RTO Algorithm

The RTO uses a gradient ascent algorithm to iteratively find the unknown optimal pointing alignment $r^\star$ which maximizes power generation. Since the logarithm of the power function (3) is concave, the power is maximized when the gradient is zero $\nabla \log P = 0$. The RTO dynamics ascend the gradient

$$r_{k+1} = r_k + F \nabla \log P(y_k) \tag{5a}$$

$$r_k = r_k \tag{5b}$$

where the current estimate $r_k \in \mathbb{R}^2$ of the optimal pointing alignment $r^\star$ is both the state and output of the RTO controller, and the input is the estimated gradient $\nabla \log P(y_k)$ of the power (3) at the current alignment y_k. The RTO (5) is a purely integral controller.

The objective of this paper is to tune the gain $F \in \mathbb{R}^{2\times 2}$ of the RTO controller (5). The gain F can be interpreted as a step-size for the gradient ascent optimization

algorithm. If this gain is not properly tuned then the RTO will not converge to the optimal pointing alignment $r^\star$. This issue is exacerbated by the fact that the RTO is operating in closed-loop with a dynamic system (2) rather than merely a static cost function (3). Thus, the RTO gain must be tuned to stabilize the closed-loop system (2) and (5) with the non-linearity (3) as shown in Fig. 1. Finally, we need to consider the parametric uncertainty of the power function (3), which can negatively effect stability and performance. This paper investigates the problem of tuning the RTO gain to provide stability, minimize alignment time, and ensure robustness to parametric uncertainty in the power function (3).

2.5 Control Objectives and Assumptions

This section formally defines the RTO tuning problem and our assumptions on this problem.

Problem 1. *Tune the gain $F \in \mathbb{R}^{2\times 2}$ of the* RTO (5) *to achieve the following control objectives:*

(a) Stabilize the closed-loop system shown in Fig. 1 with heliostat dynamics (2)*, power function* (3)*, and* RTO *controller* (5)*.*

(b) Ensure that the heliostat (2) *converges $y_k \to r^\star$ to the optimal pointing alignment $r^\star$ which maximizes power generation.*

(c) Minimize the settling-time to reach the optimal pointing alignment $r^\star$.

(d) Ensure robustness to the parametric uncertainty (4) *of the solar power function* (3)*.*

To meet these control objectives, we make the following assumptions about the RTO tuning problem.

Assumption 1.

(a) *The heliostat dynamics are Schur stable and have identity steady-state gain* $C(I-A)^{-1}B = I$.

(b) *The intensity of light across the sunspot has a Gaussian distribution* (3).

(c) *The noise* $\nu_k = \log \bar{P}_k$ *is slowly varying with respect to the gathered data.*

(d) *The gradient* $\nabla \log P(y_k)$ *is estimated without error.*

Assumption 1(a) is reasonable since the heliostats are controlled by an inner-loop controller that points the heliostats in the desired reference direction. Assumption 1(b) is consistent with experimental observations of the sunspot profile for heliostats with a single facet. However, errors in facet installation could result in multiple peaks in the sunlight intensity. Assumption 1(c) is reasonable since the power fluctuations are cause by phenomenon like the movement of clouds which are slow relative to our data-acquisition rate. Assumption 1(d) is made since the focus of this paper is to tune the gain F for stability and robustness, not to validate the gradient estimator.

3 Optimal Tuning of the RTO

In this section, we describe conditions on the RTO gain F so that the RTO algorithm maximizes power, minimizes settling-time, and provides robustness to uncertainty.

3.1 Linearity of Closed-loop Dynamics

Our key insight is that the nonlinear system depicted in Fig. 1 is equivalent to a fully linear system under Assumption 1(d) since the gradient $\nabla \log P = -\Sigma^{-1}(y_k - r^\star)$ of the logarithm of the Gaussian power distribution (3) reduces to an uncertain linear gain -Σ^{-1} acting on the heliostat dynamics output y_k and unknown optimal

reference $r^\star$. Thus, the three nonlinear blocks in Fig. 1 (the power function (3), the logarithm $\log P$, and gradient $\nabla \log P$) can be replaced by a linear gain block as shown in Fig. 3. In the block diagram shown in Fig. 3, we consider the unknown optimal pointing alignment $r^\star$ as a exogenous signal whose influence must be rejected to reach the optimal pointing alignment. We are choosing to treat the optimal pointing alignment $r^\star$ as a disturbance that can be rejected for analysis as shown in the next section.

Taking the log of the power distribution (3) and then finding the spatial gradient produces a signal $-\Sigma^{-1}(y - r^*)$. This allows us to treat the shape matrix Σ^{-1} as a linear gain and optimal pointing alignment $r^\star$ as a disturbance shown in Fig. 3

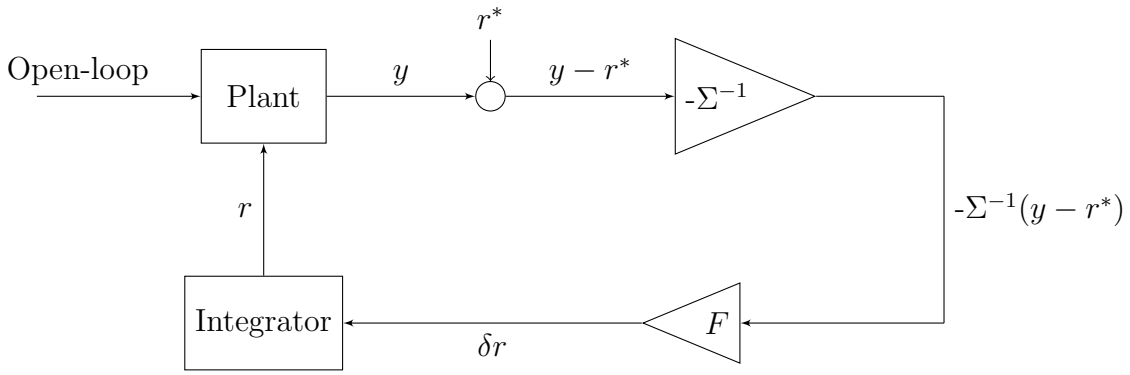

Figure 3: Block Diagram Transformation. This figure shows the transformation treating the shape matrix Σ^{-1} as a linear gain and optimal pointing alignment $r^\star$ as a disturbance.

For the linear system shown in Fig. 3, the dynamics of the closed-loop system have the state-space realization

$$\begin{bmatrix} x_{k+1} \\ r_{k+1} \end{bmatrix} = \begin{bmatrix} A & B \\ -F\Sigma^{-1}C & I \end{bmatrix} \begin{bmatrix} x_k \\ r_k \end{bmatrix} + \begin{bmatrix} 0 \\ F\Sigma^{-1} \end{bmatrix} r^* \tag{6}$$

which includes the heliostat dynamics (2), RTO dynamics (5), and the gradient $-\Sigma^{-1}(y - r^\star)$, which is equivalent to the gradient of the logarithm of the power (3). The state of the closed-loop dynamics is comprised of the states x_k and r_k of the

heliostat and RTO controller, respectively. The linear dynamics (6) will be used to optimize closed-loop performance and robustness.

3.2 Condition for Optimal Pointing Alignment

In this section, we show that the equilibrium of the closed-loop system (6) in Fig. 3 maximizes power generation. The following proposition shows that the equilibrium of the closed-loop system (6) corresponds the optimal pointing alignment of the heliostat $y_\infty = r^\star$.

Proposition 1. *Let Assumption 1 hold. Then, for any non-zero gain $F \neq 0$,*

$$(x_\infty, r_\infty) = ((I - A)^{-1}Br^*, r^*) \tag{7}$$

is the equilibrium of the system.

Proof. The equilibrium states of the heliostat x_∞ and controller r_∞ satisfy the equilibrium condition

$$\begin{bmatrix} x_\infty \\ r_\infty \end{bmatrix} = \begin{bmatrix} A & B \\ -F\Sigma^{-1}C & I \end{bmatrix} \begin{bmatrix} x_\infty \\ r_\infty \end{bmatrix} + \begin{bmatrix} 0 \\ F\Sigma^{-1} \end{bmatrix} r^*$$

This produces the solutions $x_\infty = (I - A)^{-1}Br_\infty$ and $F\Sigma^{-1}C(I - A)^{-1}Br_\infty = F\Sigma^{-1}r^\star$. Since $C(I - A)^{-1}B = I$ by Assumption 1(a), this simplifies to $F\Sigma^{-1}r_\infty = F\Sigma^{-1}r^\star$. Thus, for $F \neq 0$, we have $r_\infty = r^\star$. □

Proposition 1 shows that any non-zero gain $F \neq 0$ ensures that the equilibrium of the closed-loop system (6) maximizes power generation. Thus, a gain $F \neq 0$ will satisfy control objective 1(b), that the equilibrium of the heliostat is the optimal pointing alignment $r^\star$ which maximizes power. In subsequent sections, we will provide conditions on the gain F to provide fast and robust convergence to the equilibrium (7).

3.3 Convergence to Optimal Pointing Alignment

In this section, we show that there exists a gain F that stabilizes the closed-loop system (6). This is a necessary initial step to establish the feasibility of optimizing the RTO gain.

Lemma 1. *Let Assumption 1 hold. Then, there exists a gain $F \succeq 0$ such that the equilibrium* (7) *is stable.*

Proof. By Proposition 1, $(x_\infty, r_\infty) = ((I - A)^{-1}Br^*, r^*)$ is the equilibrium of the system. We will use the Small-gain theorem to the prove stability of this equilibrium for a sufficiently small-gain F.

The Small-gain theorem states that two stable systems connected in a feedback loop are closed-loop stable if the product of the $\mathcal{H}_\infty$-norms of the two systems is less than one [13]. The two systems in this case are the plant P and the controller C. However, the following problems occur:

i) The reference r and the actual position y are not in l_2 since the desired y_k equals r_k and equals the optimal pointing alignment $r^\star$ for all time steps k.

ii) $\|C\|_{\mathcal{H}_\infty} = \infty$ since the RTO controller (5) is an integral controller.

To solve these two problems, we will use a change of variables. We define

$$\tilde{y}_k = y_k - r_k \tag{8a}$$

$$\delta r_k = r_{k+1} - r_k \tag{8b}$$

where $\tilde{y}_k$ is the error between the heliostat's position y_k and the reference r_k, at time k and δr_k is the change in the reference between times k and $k+1$.

3.3.1 Transformed Plant

To transform the plant using (8a) and (8b), the state tracking error is defined as

$$\tilde{x}_k = x_k - \bar{x}_k \tag{9}$$

where $\bar{x}_k = (I-A)^{-1}Br_k$ is the equilibrium corresponding to the reference r_k. Using (9), the heliostat state-space realization (2) becomes

$$\tilde{x}_{k+1} = Ax_k + Br_k - (I-A)^{-1}Br_{k+1}$$

which simplifies to $\tilde{x}_{k+1} = A\tilde{x}_k - (I-A)^{-1}B\delta r_k$, where $Br_k = -A(I-A)^{-1}Br_k + (I-A)^{-1}Br_k$ since $A(I-A)^{-1} = (I-A)^{-1}A$ using (8b). Furthermore, we have $C\tilde{x}_k = Cx_k - C(I-A)^{-1}Br_k = \tilde{y}_k$ where $C(I-A)^{-1}B = I$ by Assumption 1(a) which is equivalent to (8a). This results in the transformed plant $\tilde{P}$ having a state-space realization

$$\tilde{P} = \left[\begin{array}{c|c} A & -(I-A)^{-1}B \\ \hline C & 0 \end{array}\right] \tag{10}$$

Since the matrix A is Schur and δr and $\tilde{y}$ are in l_2, the transformed plant $\tilde{P}$, has a finite H_∞-norm $\|\tilde{P}\|_{\mathcal{H}_\infty} < \infty$

3.3.2 Transformed Controller

To transform the controller (5) using (8a) and (8b), the reference error is defined as

$$\tilde{r}_k = r_k - r^* \tag{11}$$

implying $\tilde{r}_{k+1} = r_{k+1} - r^*$. This means $\tilde{r}_{k+1} = r_k - F\Sigma^{-1}y + F\Sigma^{-1}r^* - r^*$. This simplified to $\tilde{r}_{k+1} = (I - F\Sigma^{-1})\tilde{r}_k - F\Sigma^{-1}\tilde{y}_k$. Applying (8b) gives $\delta r_k = r_{k+1} - r_k =$

$(I - F\Sigma^{-1})\tilde{r}_k - F\Sigma^{-1}\tilde{y}_k$, simplifying to $\delta r_k = -F\Sigma^{-1}\tilde{r}_k - F\Sigma^{-1}\tilde{y}_k$. This results in the transformed controller $\tilde{C}$ having a state-space realization

$$\tilde{C} = \left[\begin{array}{c|c} I - F\Sigma^{-1} & -F\Sigma^{-1} \\ \hline -F\Sigma^{-1} & -F\Sigma^{-1} \end{array}\right] \tag{12}$$

It will be shown that the $\mathcal{H}_\infty$-norm of the transformed controller $\tilde{C}$ can be made arbitrarily small with the proper choice of F. First, we note that for (12) to be stable, we need $I - F\Sigma^{-1}$ to be Schur $I - F\Sigma^{-1} \preceq I$. This implies the symmetric matrix $F \succeq 0$ is positive definite.

To establish the existence of a stabilizing gain F, we will make the sub-optimal simplification $F = \beta\Sigma$. Then, by the discrete-time KYP lemma [9], $\|\tilde{C}\|_{\mathcal{H}_\infty} < \gamma$ is true if the following matrix inequality is satisfied:

$$\begin{bmatrix} (1-(1-\beta)^2)I & \beta(1-\beta)I \\ \beta(1-\beta)I & (\gamma^2 - \beta^2)I \end{bmatrix} \geq \beta^2 \begin{bmatrix} I & I \\ I & I \end{bmatrix}$$

where $P = I$ is chosen for simplicity. Via Schur complements, this matrix inequality holds if and only if the following two conditions are true:

i) $1 - (1-\beta)^2 - \beta^2 \geq 0$

ii) $\gamma^2 - 2\beta^2 - \frac{\beta^2(1-2\beta)^2}{1-(1-\beta)^2-\beta^2} \geq 0$

Conditions (i) and (ii) imply $\beta(1-\beta) \geq 0$ and $\gamma^2 \geq \frac{\beta^2}{2\beta(1-\beta)}$, respectively. Rearranging, we obtain the bounds $\beta \in [0,1]$ and $\beta \leq \frac{2\gamma^2}{1+2\gamma^2} < 1$, respectively. Choosing $\gamma < \frac{1}{\|\tilde{P}\|_{H_\infty}}$ and $\beta = \frac{2\gamma^2}{1+2\gamma^2}$ means that $\|\tilde{C}\|_{\mathcal{H}_\infty}\|\tilde{P}\|_{\mathcal{H}_\infty} < 1$. Therefore, by the Small-gain theorem, we conclude that the closed-loop is stable. □

Lemma 1 shows that there exists a gain $F \succeq 0$ such that the equilibrium (7) is stable. Therefore, Lemma 1 satisfies control objective 1(a), that the closed-loop system (6) is stabilizable. The proof of Lemma 1 is constructive, producing a gain

$F = \frac{2}{\|\tilde{P}\|^2_{H_\infty}+2}\Sigma$. However, there are two issues with this gain. First, as we will illustrate in Section 4, this gain is conservative, producing slow convergence to the optimal pointing alignment $r^\star$. In the next section, we will present a method for tuning this gain to improve settling-time. Second, this gain depends on the unknown and uncertain shape matrix Σ^{-1}. In Section 3.5, we will show how to design the gain F for robustness to the shape matrix Σ^{-1}. Nonetheless, Lemma 1 establishes that the RTO tuning problem is feasible.

3.4 Tuning the RTO to Minimize Alignment Time

In this section, we pose the problem of tuning the RTO to minimize alignment time as a LMI. First, we show that the closed-loop system (6) can be re-posed as a static output feedback (SOF) design problem. The closed-loop dynamics (6) can be factorized around the gain F to produce

$$x_{k+1} = \left(\begin{bmatrix} A & B \\ 0 & I \end{bmatrix} + \begin{bmatrix} 0 \\ I \end{bmatrix} F \begin{bmatrix} -\Sigma^{-1}C & 0 \end{bmatrix} \right) x_k \tag{13}$$

which produces the closed-loop dynamics (6). Thus, closed-loop dynamics (6) can be re-interpreted as output feedback with the open-loop state-space realization

$$\left[\begin{array}{c|c} \hat{A} & \hat{B} \\ \hline \hat{C} & 0 \end{array}\right] = \left[\begin{array}{cc|c} A & B & 0 \\ 0 & I & I \\ \hline -\Sigma^{-1}C & 0 & 0 \end{array}\right] \tag{14}$$

Therefore, the problem of tuning the RTO gain can be posed as an output feedback problem for the open-loop system (14). We adapt the LMI conditions from [3] to characterize the RTO gain that achieves exponential convergence rate α. The design procedure is summarized by the following theorem.

Theorem 1. *Let Assumption 1 hold. If the scalar $\alpha \in [0, 1)$, symmetric positive definite matrix $S \in \mathbb{R}^{6\times6}$, and matrices $G \in \mathbb{R}^{6\times6}$, $V \in \mathbb{R}^{2\times2}$, and $U \in \mathbb{R}^{2\times2}$ satisfy the* LMI

$$\begin{bmatrix} \alpha(G + G^T - S) & (\hat{A}G + \hat{B}U\hat{C})^T \\ (\hat{A}G + \hat{B}U\hat{C}) & S \end{bmatrix} \succeq 0 \tag{15a}$$

and

$$V\hat{C} = \hat{C}G \tag{15b}$$

where $\hat{A}$, $\hat{B}$, and $\hat{C}$ were defined in (14)*, then the* RTO *gain*

$$F = UV^{-1} \tag{15c}$$

exponentially stabilizes the closed-loop system (6)*.*

Proof. We will show the closed-loop system is stable using a quadratic Lyapunov function $V(x) = x^T Px$ where $P \succ 0 \in \mathbb{R}^{n\times n}$ is a positive definite matrix. We will show that the change in the Lyapunov function satisfies $\Delta V(x_k) = x_{k+1}^T Px_{k+1} - \alpha x_k^T Px_k \leq 0$ which implies that the closed-loop system (6) is exponentially stable. Substituting $FV = U$ from (15c) into the LMI (15a) yields

$$\begin{bmatrix} \alpha(G + G^T - S) & (\hat{A}G + \hat{B}FV\hat{C})^T \\ (\hat{A}G + \hat{B}FV\hat{C}) & S \end{bmatrix} \succeq 0$$

Substituting $V\hat{C} = \hat{C}G$ from (15b) into the above LMI yields

$$\begin{bmatrix} \alpha(G + G^T - S) & (\hat{A}G + \hat{B}F\hat{C}G)^T \\ (\hat{A}G + \hat{B}F\hat{C}G) & S \end{bmatrix} \succeq 0$$

which is equivalent to

$$\begin{bmatrix} \alpha(G + G^T - S) & G^T(\hat{A} + \hat{B}F\hat{C})^T \\ (\hat{A} + \hat{B}F\hat{C})G & S \end{bmatrix} \succeq 0.$$

Using the condition $G^T S^{-1} G \succeq G^T + G - S$ from [3], we obtain

$$\begin{bmatrix} \alpha(G^T S^{-1} G) & G^T(\hat{A} + \hat{B}F\hat{C})^T \\ (\hat{A} + \hat{B}F\hat{C})G & S \end{bmatrix} \succeq \begin{bmatrix} \alpha(G + G^T - S) & G^T(\hat{A} + \hat{B}F\hat{C})^T \\ (\hat{A} + \hat{B}F\hat{C})G & S \end{bmatrix} \succeq 0$$

which can be re-written as

$$\begin{bmatrix} G^T & 0 \\ 0 & I \end{bmatrix} \begin{bmatrix} \alpha S^{-1} & (\hat{A} + \hat{B}F\hat{C})^T \\ (\hat{A} + \hat{B}F\hat{C}) & S^{-1} \end{bmatrix} \begin{bmatrix} G & 0 \\ 0 & I \end{bmatrix} \succeq 0.$$

Since $I \succeq 0$ and G is full-rank, this matrix is positive semi-definite if and only if

$$\begin{bmatrix} \alpha S^{-1} & (\hat{A} + \hat{B}F\hat{C})^T \\ (\hat{A} + \hat{B}F\hat{C}) & S \end{bmatrix} \succeq 0$$

Taking the Schur complement, the LMI above is equivalent to $S^{-1} \succ 0$ and

$$\alpha S^{-1} - (\hat{A} + \hat{B}F\hat{C})^T S^{-1} (\hat{A} + \hat{B}F\hat{C}) \succeq 0$$

Substituting $P = S^{-1} \succ 0$ into the above inequality produces the Lyapunov inequality

$$\alpha P - (\hat{A} + \hat{B}F\hat{C})^T P (\hat{A} + \hat{B}F\hat{C}) \succeq 0$$

Pre and post multiplying by the closed-loop state $\hat{x}_k = (x_k, r_k)$ produces the Lya-

punov decrease condition

$$\Delta V(\hat{x}_k) = \hat{x}_k^T(\hat{A} + \hat{B}F\hat{C})^T P(\hat{A} + \hat{B}F\hat{C})\hat{x}_k - \alpha \hat{x}_k^T P \hat{x}_k \leq 0$$

which implies that the closed-loop system (6) is exponentially stable. □

Theorem 1 provides a convex characterization of the RTO gain $F = UV^{-1}$ that exponentially stabilize the closed-loop system (6). The exponential decay factor $\alpha \in [0, 1) \subset \mathbb{R}$ can be interpreted as the slowest pole of the closed-loop system. This factor α determines the rate at which the RTO drives the heliostat to the optimal pointing alignment $r^\star$. This convergence rate can be optimized using the following optimization problem.

$$\begin{aligned} \min \quad & \alpha^2 && \text{(16a)} \\ \text{s.t.} \quad & S \succ 0 && \text{(16b)} \\ & (15) && \text{(16c)} \end{aligned}$$

Although the optimization problem (16) is non-convex in both α and S, we can use a line-search to iteratively optimize α. Therefore, Theorem 1 and (16) satisfy control objective 1(c).

It is tempting to simplify the tuning problem (15) by setting $G = S$. However, as the following proposition shows, this simplification is infeasible.

Proposition 2. *If $G = S$ then $\alpha = 1$ and $F = 0$ is the only feasible solution of (15).*

Proof. Consider partitioning the Lyapunov matrix S into

$$S = \begin{bmatrix} S_{11} & S_{12} \\ S_{12}^T & S_{22} \end{bmatrix} \succ 0$$

where the partitions S_{11} and S_{22} correspond to the plant and controller dynamics, respectively, and S_{12} corresponds to the coupling in the closed-loop dynamics (6). Using the substitutions $BUC = BFCS$ from the proof of Theorem 1, the Schur complement of (15a) with $G = S$ is

$$0 \preceq \alpha S - (\hat{A} + \hat{B}F\hat{C})S(\hat{A} + \hat{B}F\hat{C})^T = \begin{bmatrix} * & * \\ * & (\alpha - 1)S_{11} + FCS_{12} + (FCS_{12})^T - FCS_{11}(FC)^T \end{bmatrix}$$

where the terms $*$ are inconsequential for this proof. From (15b), we have $[V\Sigma^{-1}C, 0] = [\Sigma^{-1}CS_{11}, CS_{12}]$, which implies that $CS_{12} = 0$ since Σ^{-1} is positive definite. Thus, (15a) holds for $G = S$ if and only if matrix $FCS_{11}C^TF^T \preceq (\alpha - 1)S_{11}$ i.e. the positive semi-definite matrix $FCS_{11}C^TF^T \succeq 0$ must be less than or equal to the negative semi-definite matrix $(\alpha - 1)S_{11} \preceq 0$ where $\alpha \leq 1$ and $S_{11} \succ 0$. This can only hold if these matrices are zero i.e. $\alpha = 0$ so that $(\alpha - 1)S_{11} = 0$ and $F = 0$ so that $FCS_{11}C^TF^T = 0$. □

Proposition 2 demonstrates the necessity of optimizing over the matrix $G \neq S$ in Theorem 1. A straightforward corollary of Proposition 2 is that Lyapunov function requires non-zero coupling $S_{12} = S_{21}^T \neq 0$ between the heliostat and RTO dynamics. Intuitively, this is necessary since the heliostat state x_k will diverge $x_k \not\to x_\infty(r_k)$ from its reference dependent equilibrium $x_\infty(r_k)$ when the RTO is aggressively converging to its equilibrium $r_k \to r^\star$. Likewise, the reference may diverge to drive the heliostat state closer to equilibrium. The coupling $S_{12} = S_{21}^T \neq 0$ in the Lyapunov matrix S accounts for the interaction between the heliostat and RTO dynamics.

3.5 Tuning the RTO for Robustness

For robustness, we need to design a RTO gain F that stabilizes the closed-loop system (6) for all Σ^{-1} contained in the set (4). This can be accomplished by requiring that the LMI (15a) holds for all $\Sigma^{-1}C$. However, this imposes an infinite number of constraints, making the problem (16) computationally intractable. We exploit convexity to reduce the infinite number of constraints into a finite number. Specifically, we enforce the LMI (15a) only on the vertices of the uncertainty set (4). The following corollary shows that the resulting RTO gain F is robust for all Σ^{-1} contained in the convex-hull (4).

Corollary 1.1. *Let Assumption 1 hold. If the scalar $\alpha \in [0, 1)$, symmetric positive definite matrix $S \in \mathbb{R}^{6\times 6}$, and matrices $G_i \in \mathbb{R}^{6\times 6}$, $V \in \mathbb{R}^{2\times 2}$, and $U \in \mathbb{R}^{2\times 2}$ satisfy the* LMI*s*

$$\begin{bmatrix} \alpha(G_i + {G_i}^T - S) & (\hat{A}G_i + \hat{B}U\hat{C}_i)^T \\ (\hat{A}G_i + \hat{B}U\hat{C}_i) & S \end{bmatrix} \succeq 0 \tag{17a}$$

and

$$V\hat{C}_i = \hat{C}_i G_i \tag{17b}$$

for $i = 1, \ldots, N$, where $\hat{A}$, $\hat{B}$ were defined in (14) *and $\hat{C}_i = \begin{bmatrix} \Sigma_i^{-1}C & 0 \end{bmatrix}$, then the* RTO *gain $F = UV^{-1}$* (15c) *exponentially stabilizes the closed-loop system* (6) *for all Σ^{-1} in the set* (4)*.*

Proof. Consider the LMIs (17a) for the vertices Σ_i^{-1} of the uncertainty set (4)

$$\begin{bmatrix} \alpha(G_i + {G_i}^T - S) & (\hat{A}G_i + \hat{B}U\hat{C}_i)^T \\ (\hat{A}G_i + \hat{B}U\hat{C}_i) & S \end{bmatrix} \succeq 0.$$

Substituting $F = UV^{-1}$ from (15c) and $V\hat{C}_i = \hat{C}_i G_i$ from (17b) gives

$$\begin{bmatrix} \alpha(G_i + {G_i}^T - S) & G_i^T(\hat{A} + \hat{B}F\hat{C}_i)^T \\ (\hat{A} + \hat{B}F\hat{C}_i)G_i & S \end{bmatrix} \succeq 0.$$

Using the condition $G^T S^{-1} G \succeq G^T + G - S$ from [3], we obtain

$$\begin{bmatrix} \alpha(G_i^T S^{-1} G_i) & G_i^T(\hat{A} + \hat{B}F\hat{C}_i)^T \\ (\hat{A} + \hat{B}F\hat{C}_i)G_i & S \end{bmatrix} \succeq \begin{bmatrix} \alpha(G_i + {G_i}^T - S) & G_i^T(\hat{A} + \hat{B}F\hat{C}_i)^T \\ (\hat{A} + \hat{B}F\hat{C}_i)G_i & S \end{bmatrix} \succeq 0$$

which can be re-written as

$$\begin{bmatrix} G_i^T & 0 \\ 0 & I \end{bmatrix} \begin{bmatrix} \alpha S^{-1} & (\hat{A} + \hat{B}F\hat{C}_i)^T \\ (\hat{A} + \hat{B}F\hat{C}_i) & S \end{bmatrix} \begin{bmatrix} G_i & 0 \\ 0 & I \end{bmatrix} \succeq 0.$$

Since $I \succeq 0$ and G_i is full-rank for all $i = 1, \ldots, N$, this matrix is positive semi-definite if and only if

$$\begin{bmatrix} \alpha S^{-1} & (\hat{A} + \hat{B}F\hat{C}_i)^T \\ (\hat{A} + \hat{B}F\hat{C}_i) & S \end{bmatrix} \succeq 0.$$

Taking an arbitrary convex combination with $\xi_i \geq 0$ and $\sum_{i=1}^N \xi_i = 1$, we obtain

$$\sum_{i=1}^N \xi_i \begin{bmatrix} \alpha S^{-1} & (\hat{A} + \hat{B}F\hat{C}_i)^T \\ (\hat{A} + \hat{B}F\hat{C}_i) & S \end{bmatrix} = \begin{bmatrix} \alpha S^{-1} & \big(\hat{A} + \hat{B}F\hat{C}(\xi)\big)^T \\ \big(\hat{A} + \hat{B}F\hat{C}(\xi)\big) & S \end{bmatrix} \succeq 0$$

where we define $\hat{C}(\xi) = \sum_{i=1}^N \xi_i \hat{C}_i$. Taking the Schur complement, we obtain

$$\alpha S^{-1} - \big(\hat{A} + \hat{B}F\hat{C}\Sigma(\xi)^{-1}\big)^T S^{-1} \big(\hat{A} + \hat{B}F\hat{C}\Sigma(\xi)^{-1}\big) \succeq 0$$

where any shape-matrix Σ in the convex-hull (4) can be expressed as the convex

combination $\Sigma^{-1}(\xi) = \sum_{i=1}^{N} \xi_i \Sigma_i^{-1}$ of the vertices Σ_i^{-1}. Substituting $P = S^{-1} \succ 0$, we obtain the Lyapunov inequality

$$\alpha P - (\hat{A} + \hat{B}F\hat{C}\Sigma^{-1})^T P(\hat{A} + \hat{B}F\hat{C}\Sigma^{-1}) \succeq 0$$

for any Σ^{-1} in the set (4). Thus, according to Theorem 1, the closed-loop system is exponentially stable for all shape matrix Σ^{-1} contained in the set (4). □

Corollary 1.1 shows that the infinite number of constraints imposed by the shape matrix Σ^{-1} can be reduced by taking advantage of convexity. This allows us to produce a gain F that is robust to the shape of the power distribution (3). Therefore Corollary 1.1 satisfies control objective 1(d) to ensure robustness to the parametric uncertainty of the power function (3).

4 Simulations and Results

In this section, we illustrate the presented method for tuning the RTO gain F. We will compare convergence rates of the optimized RTO gain F with the conservative gain presented in Lemma 1. We will compare robustness of the gain F tuned using (4) with non-robust optimization-based tuning (16).

4.1 Numerical Details

In this section, we numerically define the parameters used for our simulations of the closed-loop system with the RTO algorithm.

4.1.1 Heliostat Dynamics

The heliostat dynamics (2) are modeled as

$$H(s) = \begin{bmatrix} H_{az,az}(s) & H_{az,el}(s) \\ H_{el,az}(s) & H_{el,el}(s) \end{bmatrix}$$

where azimuth and elevation angle directions of the heliostat are assumed to be uncoupled $H_{az,el}(s) = H_{el,az}(s) = 0$. The azimuth and elevation angle directions each have their own general second order transfer function

$$H_i(s) = \frac{{\omega_n}^2}{s^2 + 2\zeta\omega_n s + {\omega_n}^2 + {\omega_n}^2 u}$$

for both azimuth $i = az, az$ and elevation $i = el, el$ angle, where $\zeta_{az} = 1.1$, $\zeta_{el} = 0.9$, $\omega_{n,az} = \frac{1}{10}$, and $\omega_{n,el} = \frac{1}{20}$. Since $\zeta_{az} = 1.1 > 1$, the dynamics are over-damped, reflecting the typical design of the inner-loop servos on the heliostats. An under-damped ζ_{el} was chosen to demonstrate that the system can stabilize with different damping ratios between the two directions. The natural frequencies ω_n were chosen to represent the time the heliostats take to move in each direction. The values ζ and ω_n differ between each direction to simulate possible differences between the azimuth and elevation angle transfer functions.

The heliostat model $H(s)$ was converted into discrete time with a sample time of 6 seconds. For each simulation, $r_0 \neq r^\star$ is the alignment provided by the operator. However, this alignment is non-optimal due to uncertainty about the heliostat position and encoder errors.

4.1.2 Power Distributions

Two power functions (3) will be used to simulate the RTO algorithm. Each power distribution is representative of a sunspot that can be encountered at a CSP plant.

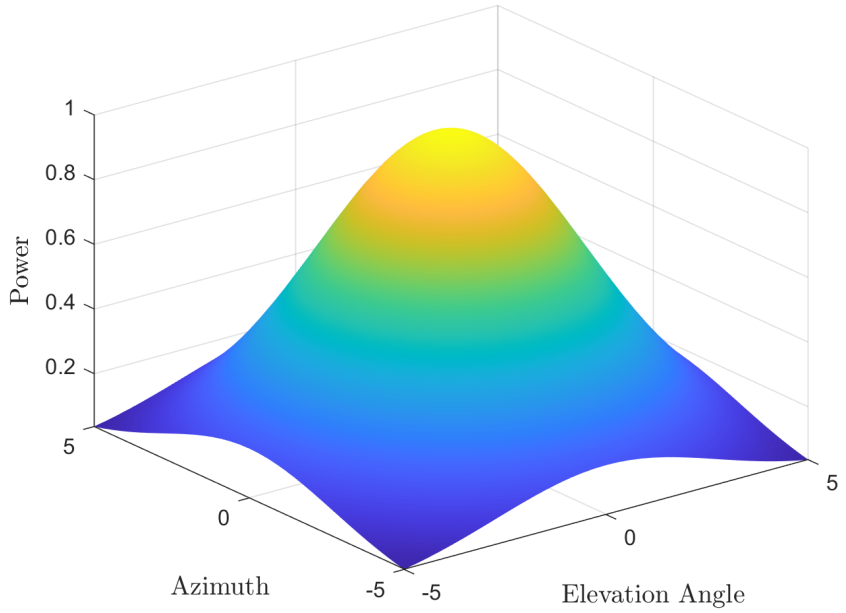

Figure 4: Example Power Distribution. This figure shows the power intensity $P(y)$ at a given y_{az} and y_{el}.

The power distribution (3) shown in Fig. 4 is an example of a distribution that is used in the simulations. The distributions used in the simulations are viewed from the top to show clear differences between them. The example distribution is meant to give context for the power intensity at each azimuth and elevation angle for the distributions.

The power distributions in Fig. 5 are used to simulate the RTO algorithm with an ideal (left) and a non-ideal (right) situation. The matrices Σ for these power distributions are $\Sigma = \begin{bmatrix} 7.5 & 0 \\ 0 & 7.5 \end{bmatrix}$ and $\Sigma = \begin{bmatrix} 10 & 4 \\ 4 & 5 \end{bmatrix}$, respectively. The optimal reference $r^\star$ is the origin $r^\star = (0, 0)$. The power in the simulations is represented as a percentage for clarity. These choices are made without loss of generality to ensure the clarity of the plots. The optimal reference $r^\star$ and maximum power intensity $P(r^\star)$ are known in order to validate the RTO algorithm. In practice, the optimal pointing alignment $r^\star$ and maximum power intensity $P(r^\star)$ will be unknown. The ideal

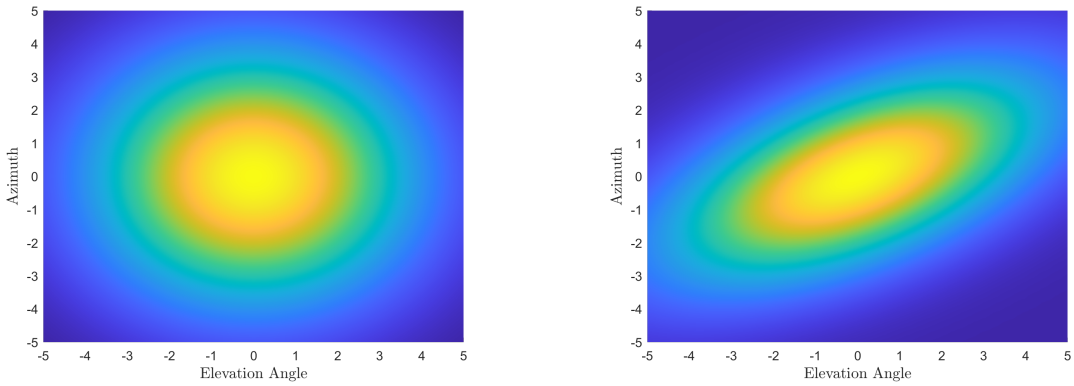

(a) (b)

Figure 5: Normal Distribution (left) and Oblong Distribution (right). This figure shows the power intensity $P(y)$ at a given y_{az} and y_{el}.

power distribution can be encountered when the Sun is above the heliostat and the heliostat is inline with the receiver, causing better focusing of the sunspot on the receiver. The non-ideal power distribution can be encountered when the Sun is not inline or directly above the heliostat, causing the sunspot to be stretched on the receiver.

4.1.3 Gradient Estimator

For our simulations, a BLS algorithm was used to estimate the gradient. Using the first-order Taylor series expansion

$$\log P_i \approx \log P(\bar{y}) + \nabla \log P(\bar{y})^T (y_i - \bar{y}) = \theta^T \phi_i$$

where the parameter θ and regressor ϕ vectors are defined as

$$\phi_i = \begin{bmatrix} 1 \\ y_i - \bar{y} \end{bmatrix} \text{ and } \theta = \begin{bmatrix} \log P(\bar{y}) \\ \nabla \log P(\bar{y}) \end{bmatrix}$$

allow us to use the real-time dataset $(\log P_i, y_i)$ to estimate the gradient $\nabla \log P(\bar{y})$ at the current alignment $\bar{y}$. The parameters θ are estimated using the BLS estimator $\hat{\theta} = (\Phi\Phi^T)^{-1}\Phi P$ where $\Phi = \begin{bmatrix} \phi_1 & ... & \phi_N \end{bmatrix}$ is the batch regressor matrix and $P = \begin{bmatrix} P_1 & ... & P_N \end{bmatrix}^T$ is the batch output vector with N measurements. The estimated gradient $\nabla \log P(\bar{y})$ is pulled from the estimated parameter vector $\hat{\theta}$.

4.1.4 Controller design

The controller (5) used in the simulations requires the gain F to be computed using the shape matrices Σ^{-1} from the power distributions (3). The power distributions in Fig. 5 are used to calculate F from Theorem 1 using the MATLAB package Yalmip with the SDPT3 solver. This solver was used to solve the SDP problem (16) where (15a) $\in \mathbb{R}^{12\times 12}$. Since including α as a decision variable renders (16) non-convex, we optimize α via a line-search. We found the optimal $\alpha = 0.9999999$ which is the smallest value for which (16) is feasible. The gain F was found in 1.668338 seconds.

4.2 Destabilizing RTO

In this section, we show that the RTO (5) can destabilize the closed-loop system if the gain F is not properly tuned. The purpose of this simulation is to motivate the careful tuning procedure presented in this paper.

Fig. 6 shows the simulation results for the heliostat (2) in closed-loop with the RTO controller (5) using the power intensity (3) in Fig. 5(b) and an aggressive gain $F = 5\Sigma^{-1}$. The gradient $\nabla \log P(y_k)$ was estimated using BLS with 10 sensors in a circular configuration with radius 0.1 around the current position y_k. Thus, we are simulating the nonlinear system shown in Fig. 1 rather than the linear closed-loop system (6), which is equivalent under the assumption of perfect gradient estimation. Fig. 6 shows the time-varying estimated optimal pointing alignment r_k produced

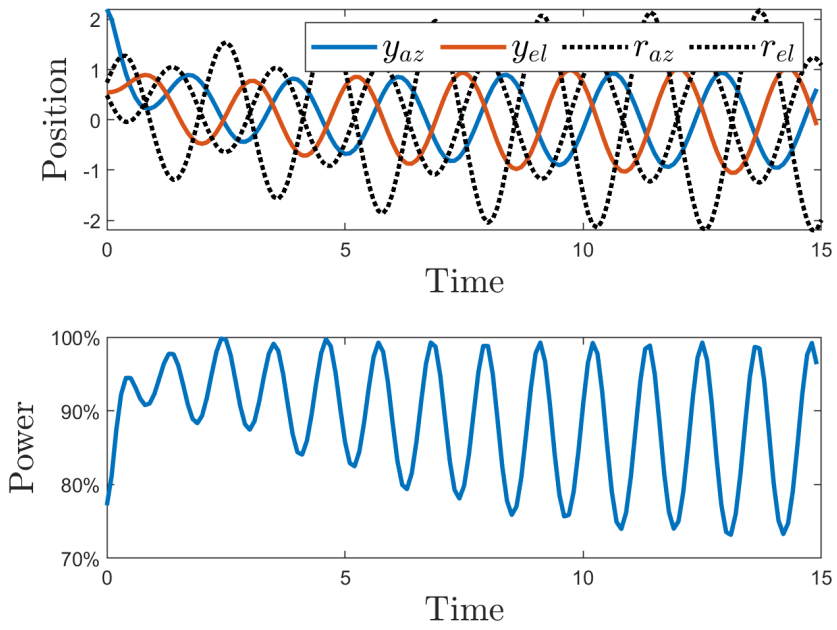

Figure 6: Oblong Distribution Simulation with Aggressive Gain. This simulation shows (y_{az}, y_{el}) and (r_{az}, r_{el}), versus time (top). The simulation also shows $P(y)$ versus time (bottom).

by the RTO (5) and the actual time-varying alignment y_k of the heliostat (2). The actual heliostat alignment y_k lags the desired alignment r_k, but both increasingly overshoot the optimal pointing alignment $y_k \to r_k \not\to 0$. Although, both the heliostat dynamics (2) and RTO gradient ascent dynamics (5) are over-damped in azimuth, we see oscillator closed-loop behavior due to the interaction of these dynamic systems; justifying the need for careful analysis of the non-trivial closed-loop dynamics. Fig. 6 shows that the power $P_k = P(y_k)$ is not converging to the maximum power $\bar{P} = 100\%$.

4.3 Conservative Convergence of RTO

In this section, we compare the performance of the RTO gain F tuned using the optimization problem (16) with the conservative gain suggested by Lemma 1. The purpose of this comparison is to illustrate that the presented tuning procedure can

reduce the settling time to the optimal pointing alignment $r^\star$ over a naive tuning.

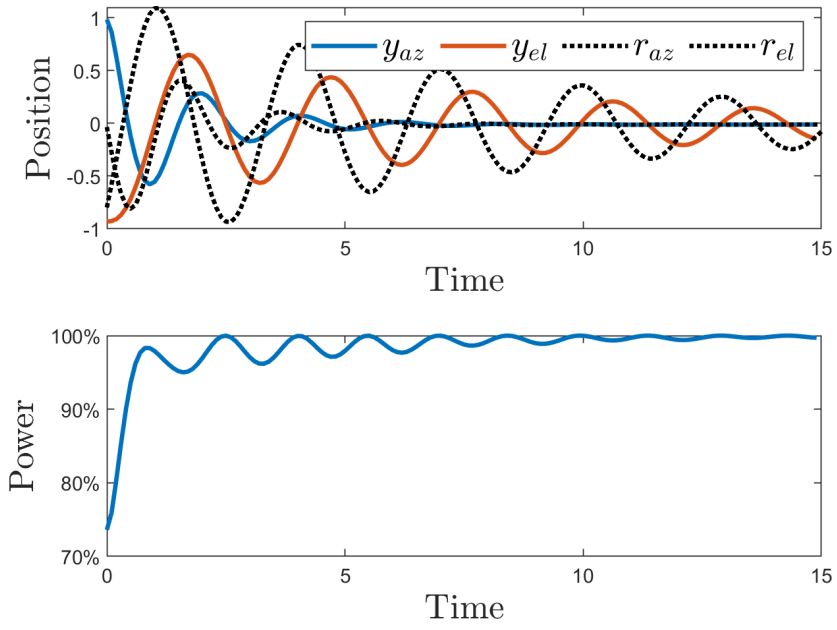

Figure 7: Simulation with Conservative Gain. This simulation shows (y_{az}, y_{el}) and (r_{az}, r_{el}), versus time (top). The simulation also shows $P(y)$ versus time (bottom).

Fig. 7 shows the simulation results for the nonlinear closed-loop system shown in Fig. 1 using the conservative gain suggested by Lemma 1. The $\mathcal{H}_\infty$-norm was computed using the MATLAB command `norm`. The power distribution (3) used in these simulation results is shown in Fig. 5(b). The gradient $\nabla \log P(y_k)$ was estimated using batch least squares, like in the previous simulation results.

Fig. 7 shows the time-varying estimated optimal pointing alignment r_k produced by the RTO algorithm (5) and the actual time-varying alignment y_k of the heliostat (2). The actual heliostat alignment y_k lags the desired alignment r_k, but both converge to the optimal pointing alignment $y_k \to r_k \to 0$. Similar to the unstable case, we see oscillator closed-loop behavior due to the interaction of the dynamic systems, the heliostat dynamics (2) and RTO controller gradient ascent dynamics (5), showing that this is not a simple gradient ascent problem and justifying the need for careful analysis of the non-trivial closed-loop dynamics. Fig. 7 shows that the

power $P_k = P(y_k)$ converges $P_k \to 100\%$ to the maximum power $\bar{P} = 100\%$. This simulation empirically validates Proposition 1 and Lemma 1. The simulation shows that the equilibrium of the closed-loop system (6) is the optimal pointing alignment $r^\star$ and that this equilibrium is able to be stabilized. Furthermore, these simulation results will help show later that the optimized gain reduces settling time to the optimal pointing alignment $r^\star$ compared with the Small-gain theorem design.

4.4 Validating Stability

In this section, we show that the gain F from Theorem 1 stabilizes the closed-loop system shown in Fig. 1 and converges faster than the conservative gain shown in Fig. 7. These simulations are also meant to show that the RTO algorithm can converge to the optimal pointing alignment $r^\star$ with an ideal and non-ideal sunspot shape. In the physical system, encountering ideal situations is rare. However, it is important to show the RTO can maximize power in ideal and non-ideal situations.

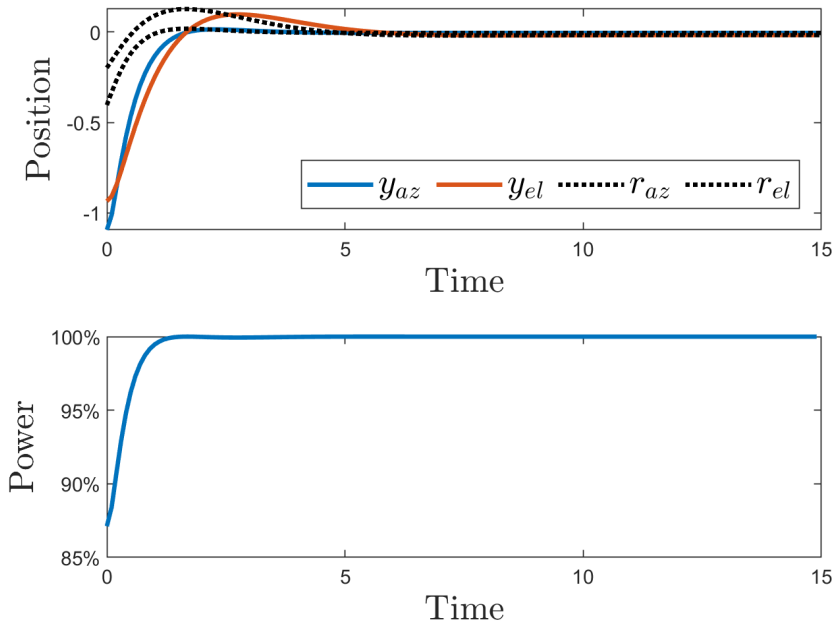

Figure 8: Normal Distribution Simulation. This simulation shows (y_{az}, y_{el}) and (r_{az}, r_{el}), versus time (top). The simulation also shows $P(y)$ versus time (bottom).

Fig. 8 shows the simulation results for the heliostat (2) in nonlinear closed-loop with the RTO controller (5) using the power intensity (3) in Fig. 5(a). The gradient $\nabla \log P(y_k)$ was estimated using batch least squares, like in the previous simulation results.

Fig. 8 shows the time-varying estimated optimal pointing alignment r_k produced by the RTO algorithm (5) and the actual time-varying alignment y_k of the heliostat (2). The actual heliostat alignment y_k lags the desired alignment r_k, but both converge to the optimal pointing alignment $y_k \to r_k \to 0$. Fig. 8 shows that the power $P_k = P(y_k)$ converges $P_k \to 100\%$ to the maximum power $\bar{P} = 100\%$.

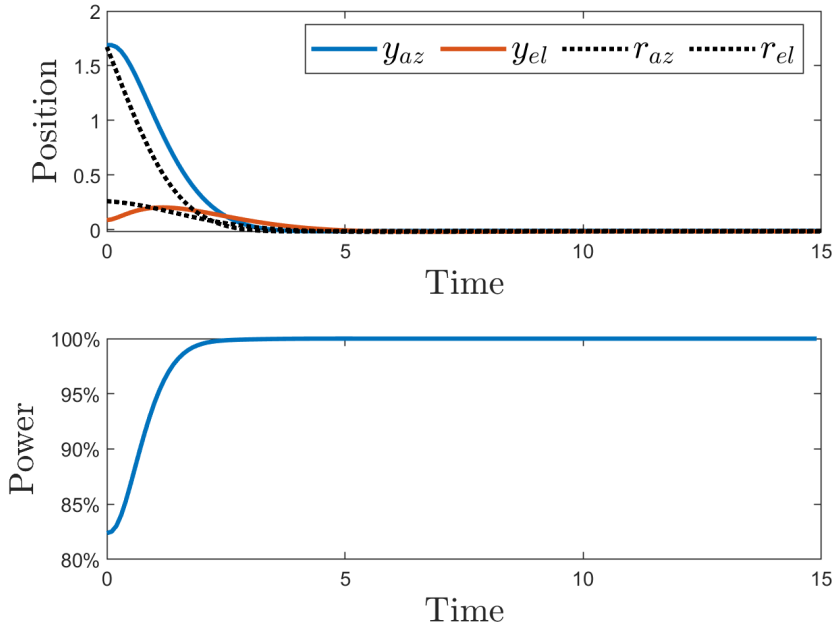

Figure 9: Oblong Distribution Simulation. This simulation shows (y_{az}, y_{el}) and (r_{az}, r_{el}), versus time (top). The simulation also shows $P(y)$ versus time (bottom).

Fig. 9 shows the simulation results for the heliostat (2) in nonlinear closed-loop with the RTO controller (5) using the power intensity (3) in Fig. 5(b). The gradient $\nabla \log P(y_k)$ was estimated using batch least squares, like in the previous simulation results.

Fig. 9 shows the time-varying estimated optimal pointing alignment r_k produced by

the RTO algorithm (5) and the actual time-varying alignment y_k of the heliostat (2). The actual heliostat alignment y_k lags the desired alignment r_k, but both converge to the optimal pointing alignment $y_k \to r_k \to 0$. Fig. 9 shows that the power $P_k = P(y_k)$ converges $P_k \to 100\%$ to the maximum power $\bar{P} = 100\%$.

These simulations empirically validate Proposition 1 and Lemma 1. The simulations show that the equilibrium of the system is the optimal pointing alignment $r^\star$ and that the equilibrium is able to be stabilized. The simulations also empirically validate Theorem 1, proving the gain F found with Theorem 1 stabilizes the closed-loop system in Fig. 1 and settles faster than the conservative gain in Fig. 7. The simulations show that the RTO algorithm will maximize power despite initial conditions with ideal and with non-ideal power distributions.

4.5 Validating Robustness

This section demonstrates the robustness of the presented RTO tuning to uncertainty in the shape matrix Σ^{-1} of the power distribution (3). The following simulations are meant to show that the RTO algorithm can converge to the optimal pointing alignment $r^\star$ regardless of the power distribution (3). In the physical system, the power distribution is not known beforehand and is difficult to predict. However, it is important to show that the system can maximize power in varying situations. The same gain F is used for each power distribution.

Fig. 10 and Fig. 11 show the simulation results for the heliostat (2) in nonlinear closed-loop with the RTO controller (5) using 25 different power distributions (3). The gradient $\nabla \log P(y_k)$ was estimated using batch least squares, like in the previous simulation results.

Fig. 10 and Fig. 11 show the actual time-varying alignment y_k of the heliostat (2). The actual heliostat alignment y_k for each power distribution (3) converge to the optimal pointing alignment $y_k \to r_k \to 0$. Fig. 10 and Fig. 11 show that the power

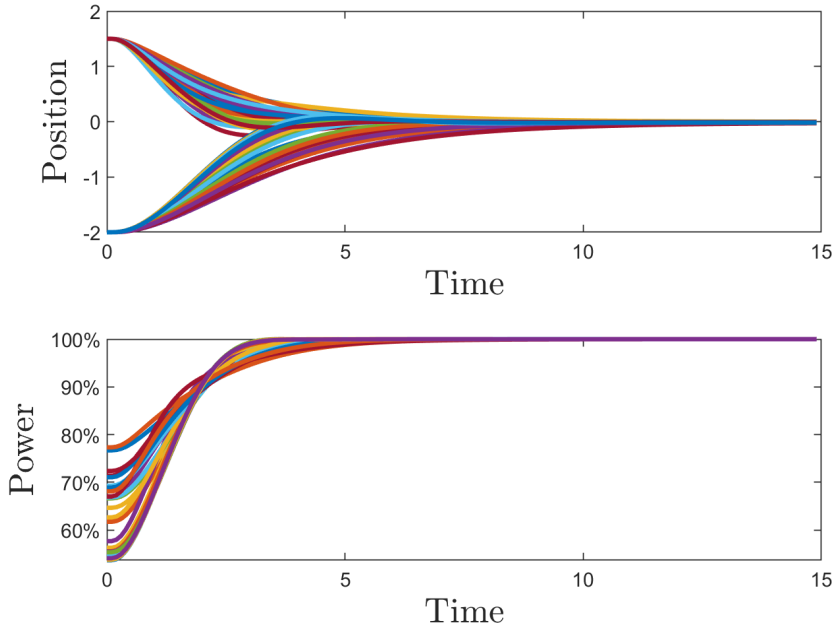

Figure 10: Robust Simulation with Constant Initial Condition. This simulation shows (y_{az}, y_{el}) versus time (top). The simulation also shows $P(y)$ versus time (bottom).

$P_k = P(y_k)$ converges $P_k \to 100\%$ to the maximum power $\bar{P} = 100\%$ for each power distribution.

These simulations validate Proposition 1 and Lemma 1, showing that the equilibrium of the system is the optimal pointing alignment $r^\star$ and showing that the equilibrium is stabilizable. These simulations also show that the gain F from Theorem 1 and tuned using (4) stabilizes the system and is robust to the power distribution (3), empirically validating robustness and Theorem 1. This means that the RTO algorithm will maximize power despite initial conditions and uncertainty in the power distributions.

4.6 Validating Solar tracking

In this section, we show that the gain F from Theorem 1 stabilizes the closed-loop system shown in Fig. 1 and tracks a moving Sun over a 12 hour period using the

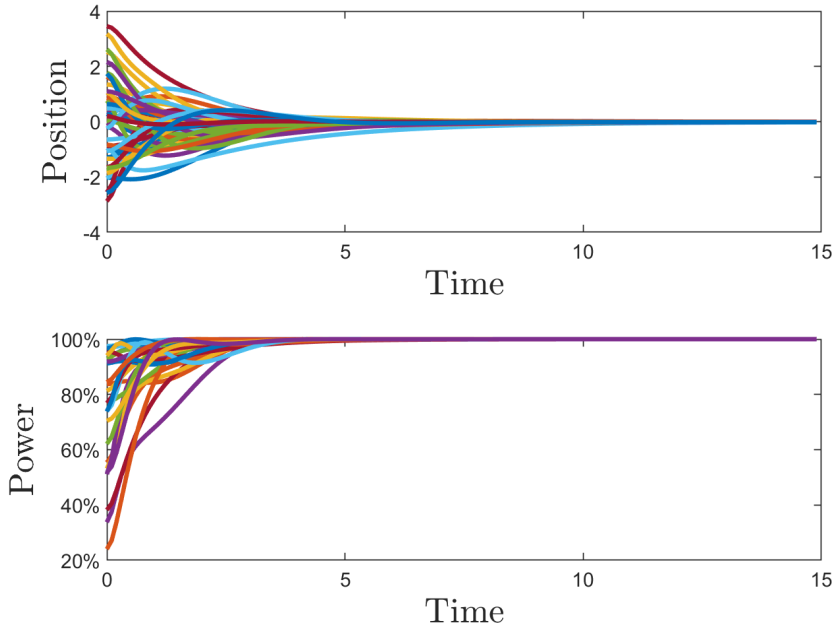

Figure 11: Robust Simulation with Random Initial Conditions. This simulation shows (y_{az}, y_{el}) versus time (top). The simulation also shows $P(y)$ versus time (bottom).

oblong distribution in Fig. 5(b). This is done by adding a sine wave with a period of 24 hours to $r^\star$ in (3). These simulations are also meant to show that the RTO algorithm can converge to the optimal pointing alignment $r^\star$ and maintain this alignment while the Sun moves throughout the day.

Fig. 12 shows the simulation results for the heliostat (2) in nonlinear closed-loop with the RTO controller (5) using the power intensity (3) in Fig. 5(b). The gradient $\nabla \log P(y_k)$ was estimated using batch least squares, like in the previous simulation results.

Fig. 12 shows the time-varying estimated optimal pointing alignment r_k produced by the RTO algorithm (5) and the actual time-varying alignment y_k of the heliostat (2). The actual heliostat alignment y_k lags the desired alignment r_k, but both converge to the optimal pointing alignment $y_k \to r_k \to r^\star$. Fig. 12 shows that the power $P_k = P(y_k)$ converges $P_k \to 100\%$ to the maximum power $\bar{P} = 100\%$.

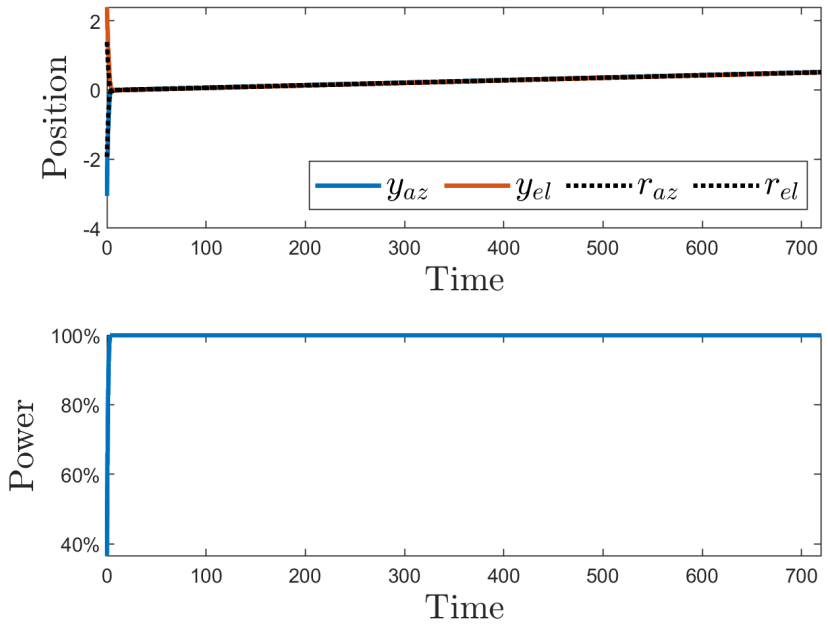

Figure 12: Solar Tracking Simulation. This simulation shows (y_{az}, y_{el}) and (r_{az}, r_{el}), versus time (top). The simulation also shows $P(y)$ versus time (bottom).

This simulation empirically validates Proposition 1 and Lemma 1. The simulation shows that the equilibrium of the system is the optimal pointing alignment $r^\star$ and that the equilibrium is able to be stabilized. The simulations also empirically validate Theorem 1, proving the gain F found with Theorem 1 stabilizes the closed-loop system in Fig. 1. The simulation shows that the RTO algorithm will maximize power despite initial conditions and movement of the Sun.

4.7 Validating Robust Solar tracking with Noise

In this section, we demonstrate the robustness of the presented RTO tuning to uncertainty in the shape matrix Σ^{-1} of the power distribution (3) and we show that the gain F from Theorem 1 stabilizes the closed-loop system shown in Fig. 1 and tracks a moving Sun over a 12 hour period despite noise. This is done by adding a sine wave with a period of 24 hours to $r^\star$ in (3) and error to the power measurements $\log P_i$. These simulations are also meant to show that the RTO algorithm can

converge to the optimal pointing alignment $r^\star$ and maintain this alignment while the Sun moves throughout the day and despite noise.

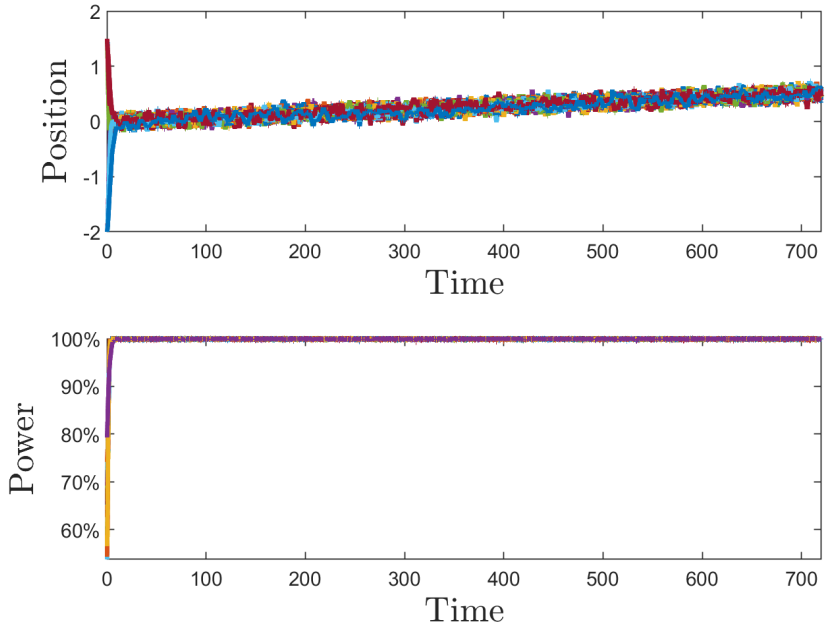

Figure 13: Solar Tracking Simulation. This simulation shows (y_{az}, y_{el}) versus time (top). The simulation also shows $P(y)$ versus time (bottom).

Fig. 13 shows the simulation results for the heliostat (2) in nonlinear closed-loop with the RTO controller (5) using the same gain F for 25 different power distributions (3). The gradient $\nabla \log P(y_k)$ was estimated using batch least squares, like in the previous simulation results.

Fig. 13 shows the actual time-varying alignment y_k of the heliostat (2). The actual heliostat alignment y_k of each power distribution (3) converge to the optimal pointing alignment $y_k \to r_k \to r^\star$. Fig. 13 shows that the power $P_k = P(y_k)$ converges $P_k \to 100\%$ to the maximum power $\bar{P} = 100\%$ for each distribution.

These simulations empirically validate Proposition 1 and Lemma 1. The simulations show that the equilibrium of the system is the optimal pointing alignment $r^\star$ and that the equilibrium is able to be stabilized. The simulations also empirically validate Theorem 1, proving the gain F found with Theorem 1 and tuned using

(4) stabilizes the closed-loop system in Fig. 1 and is robust to the power distribution (3), empirically validating robustness and Theorem 1. The simulations show that the RTO algorithm will maximize power despite initial conditions, movement of the Sun, noise, and uncertainty in the power distributions.

4.8 Physical Heliostat Test

In this section, we show results from a physical test on a single heliostat using two different set-points from a human operator. We show that the RTO algorithm realigns the heliostat to optimize power. These tests are meant to empirically validate the RTO algorithm presented in this paper using actual data and heliostat dynamics.

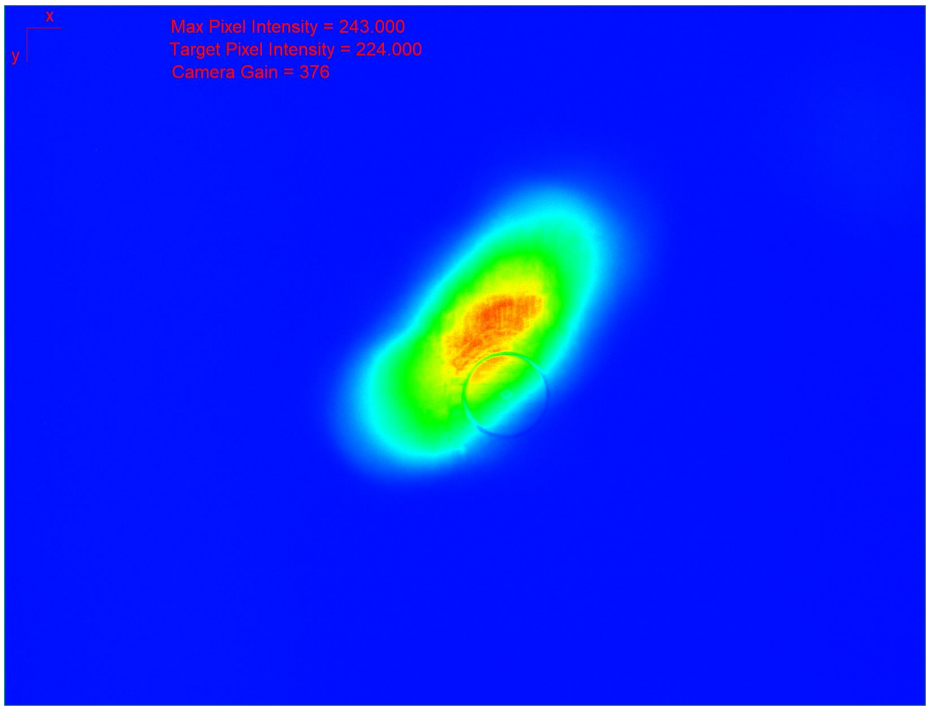

Figure 14: First Initial Offset. This figure shows the BCS image before realignment.

Fig. 14 and Fig. 15 show the heliostat alignment using the first offset before and after using the RTO algorithm. The gradient was estimated using BLS and the light intensities of each pixel from the BCS images. The relative pixel locations were

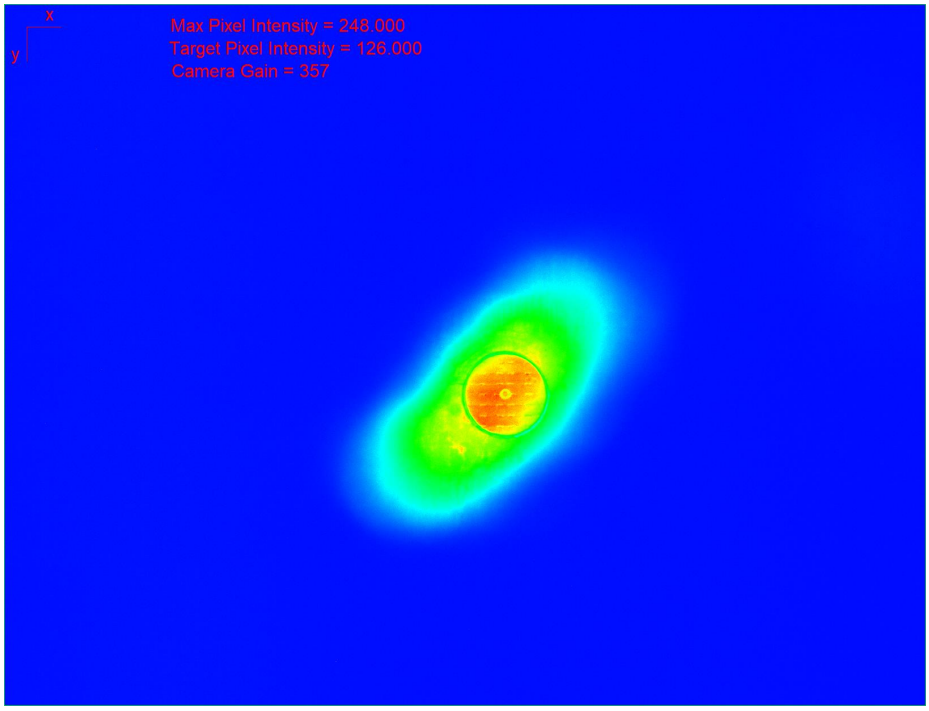

Figure 15: First Realignment. This figure shows the BCS image after using the RTO algorithm.

converted into azimuth and elevation angle positions to output new references for the heliostats to track.

Fig. 15 shows that the RTO algorithm aligns the sunspot so that the maximum power intensity is on the desired target location.

This result empirically shows that the RTO algorithm will maximize power on the receiver using an actual heliostat.

Fig. 16 and Fig. 17 show the heliostat alignment using the second offset before and after using the RTO algorithm. The gradient was estimated using BLS and the light intensities of each pixel from the BCS images. The relative pixel locations were converted into azimuth and elevation angle positions to output new references for the heliostats to track.

Fig. 17 shows that the RTO algorithm aligns the sunspot so that the maximum power intensity is on the desired target location.

This result empirically shows that the RTO algorithm will maximize power on the

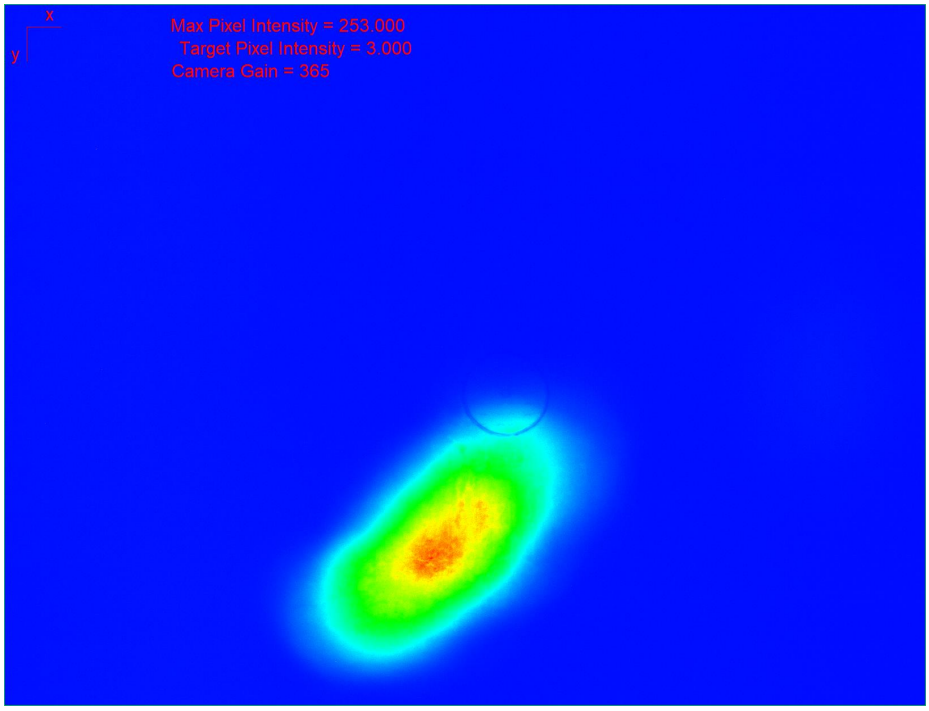

Figure 16: Second Initial Offset. This figure shows the BCS image before realignment.

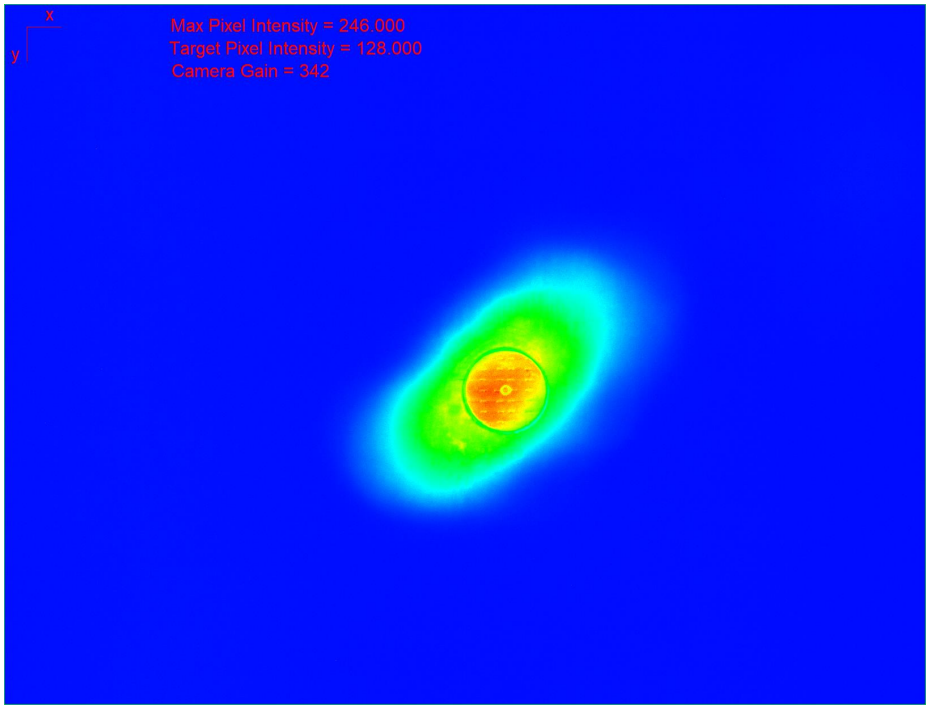

Figure 17: Second Realignment. This figure shows the BCS image after using the RTO algorithm.

receiver using an actual heliostat.

5 Conclusion

In this paper, a closed-loop approach was presented for CSP plants using heliostats and power towers. We presented an optimization-based tuning procedure that optimizes the settling time while guaranteeing stability and robustness to model uncertainty. Our method re-structures the problem as a SOF problem and uses known SOF methods to couple the Lyapunov functions of the plant (2)(3) and the controller (5) to stabilize the feedback loop. The RTO algorithm accomplishes the control objectives outlined in Problem 1. This is shown in Section 4 using a variety of power distributions (3) and using actual BCS images and heliostats. This data-driven approach uses real-time data to continually improve the heliostat alignment. Unlike other methods, our approach maximizes how much power a given CSP plant can produce by compensating for faults in hardware installation and miscalibration. The RTO algorithm also improves the heliostats' response to disturbances like wind by optimizing the settling time of the heliostat to the optimal pointing alignment $r^\star$ using data. The ability of this method to use a variety of sensors that are already a part of the infrastructure of many CSP plants and different estimators adds flexibility that lets this method be applied to various CSP plants with unique requirements.

The method presented in this paper will allow CSP using heliostats and power towers to be more competitive with non-renewable sources by not only improving efficiency and power generation, but by also reducing operation costs by minimizing the need for a human operator.

References

[1] Kartik Ariyur and Miroslav Krstic. *Real-Time Optimization by Extremum Seeking Control*. 03 2004.

[2] K. Conover. Photovoltaic operation and maintenance evaluation. *IEEE Transactions on Energy Conversion*, 5(2):279–283, 1990.

[3] J. Daafouz, P. Riedinger, and C. Iung. Stability analysis and control synthesis for switched systems: a switched lyapunov function approach. *IEEE Transactions on Automatic Control*, 47(11):1883–1887, 2002.

[4] Joshua Freeman, Keerthi K. S, and Lekshmi R. Chandran. Closed loop control system for a heliostat field. In *2015 International Conference on Technological Advancements in Power and Energy (TAP Energy)*, pages 272–277, 2015.

[5] Ali Kashani, Shirin Panahi, Ankush Chakrabarty, and Claus Danielson. Robust data-driven dynamic optimization using a set-based gradient estimator. *Optimal Control Applications and Methods*, n/a(n/a).

[6] Ali Kashani, Shirin Panahi, Ankush Chakrabarty, and Claus Danielson. Robust data-driven dynamic optimization using a set-based gradient estimator. *Optimal Control Applications and Methods*, 06 2024.

[7] Abraham Kribus, Irina Vishnevetsky, Amnon Yogev, and Tatiana Rubinov. Closed loop control of heliostats. *Energy*, 29(5):905–913, 2004. SolarPACES 2002.

[8] Benjamin Liu, Alexander Sonn, Anthony Roy, and Brian Brewington. Deep learning method for heliostat instance segmentation. *SolarPACES Conference Proceedings*, 1, Feb. 2024.

[9] Federico Najson. The kalman-yakubovich-popov lemma for discrete-time positive linear systems. In *2012 American Control Conference (ACC)*, pages 5188–5193, 2012.

[10] Lalit Singh Parmar and Sudhir Kumar Singh. A study of performance and analysis csp renewable based on solar tower power plant. In *2022 5th International Conference on Contemporary Computing and Informatics (IC3I)*, pages 1094–1099, 2022.

[11] Saeid Shokri, Reza Hayati, Mahdi Ahmadi Marvast, Ayazi Mohammad, and Ganji Hamid. Real time optimization as a tool for increasing petroleum refineries profits. *Petroleum and Coal*, 01 2009.

[12] Michael Soderstrand, Sung Lee, and Peter Chung. Mini-dish based hybrid concentrated solar power (csp) system for home use. pages 689–692, 08 2013.

[13] A.R. Teel. A nonlinear small gain theorem for the analysis of control systems with saturation. *IEEE Transactions on Automatic Control*, 41(9):1256–1270, 1996.

[14] David B. Thomas and Wayne Luk. Sampling from the multivariate gaussian distribution using reconfigurable hardware. In *15th Annual IEEE Symposium on Field-Programmable Custom Computing Machines (FCCM 2007)*, pages 3–12, 2007.

[15] W.T. Xie, Y.J. Dai, R.Z. Wang, and K. Sumathy. Concentrated solar energy applications using fresnel lenses: A review. *Renewable and Sustainable Energy Reviews*, 15(6):2588–2606, 2011.

[16] Lingxiang Yao, Yang Wang, and Xianyong Xiao. Concentrated solar power plant modeling for power system studies. *IEEE Transactions on Power Systems*, 39(2):4252–4263, 2024.